A Chamber Experiment for the Feasibility Study of an Artificial Plasma Reflector for OTH Radar Applications

Technical Report for the work supported by

NASA Grant No. NAG5-1051

S.P. Kuo
Principal Investigator

Y.S. Zhang
Q.H. Ji
P.E. Miller
K.K. Tiong

A Chamber Experiment for the Feasibility Study of an Artificial Plasma Reflector for OTH Radar Applications

It is a known fact that conventional line of sight radars are limited by their range of detection. This limitation is removed, however, by over-the-horizon (OTH) radars. OTH radars use ionospheric plasma to reflect obliquely incident radar pulses back to the ground a distance away from the radar site. The range of detection is, in general, from 2000 to 4000km which is far outside the range of line of sight. A schematic of the OTH radar arrangement is shown in Figure 1. Since the radar pulses are coming down from the ionosphere, moving targets can be detected, in principle, at any altitude. The extended range of detection of OTH radars can also be used to monitor ships and oceans from a land base. Moreover, OTH radars can also be used for air traffic control in areas where the simple line of sight radars can not reach. The above mentioned attractive applications of the OTH radars in turn generate a great deal of concern on how to improve the sensitivity of the OTH radar.

It is believed that the sensitivity of an OTH radar can be improved if the capability of the OTH radar can be extended with respect to three major factors. The first one regards the range of the radar. In order to avoid cluttering in the radar return, a large clearance region which is proportional to the height of the ionospheric reflector is required. Thus, OTH radar is, in general, blind in a zone from 1000 to 2000km which is still outside the line of sight range. The next concerns the resolution of the radar which depends strongly on the radar frequency. Since the peak electron density of the ionosphere is about $10^6 cm^{-3}$, the operating frequency of the OTH radar is limited to be in the range from 6 to 30 MHz. In addition, the long propagation length also tends to degrade the resolution of the return. The last concern is on the stability of the ionosphere, which varies from day to night. This variation will affect the performance and reliability of the radar.

These concerns may be resolved if a reflector can be positioned at a much lower altitude which is able to reflect radar pulses of much higher frequency. In addition, if the reflector is made artificially, its stability and location are controllable. Two schemes have been proposed. Both schemes use a high power RF breakdown approach for plasma generation. The RF pulses used for air breakdown and plasma maintenance will be transmitted by ground based phased array antennas. In the first scheme, only a single focused RF beam will be employed to produce an ionization patch in the D region (70 - 80km altitude) of the ionosphere. The RF beam is required to be focused because the altitude is well above the altitude of minimum

breakdown threshold. Consequently, the cross section of the beam at the patch altitude will be too small in comparison with the Fresnel size, and a scanning process must be incorporated in the operation of the RF beam in order to enlarge and tilt the ionization patch. The density of the patch is expected to be at the same level as that of the F-peak (ie $n_e \cong 10^6 cm^{-3}$) and thus, the same radar (ie existing OTH radar) can be used in the operation. The schematic arrangement of this scheme is shown in Figure 2. The radar resolution may still be improved since the reflector is located at a much lower height. The major technical difficulties of the scheme appear to be how to uniformly enlarge and tilt the ionization patch.

The second scheme can, however, remedy these difficulties. Two crossed beams are proposed to be used for plasma generation in their intersection region, at an altitude between 30 and 60km. The interference between the fields of the two beams enhances the peak field amplitude and, thus, reduces the required power level of each RF beam. This, in turn, helps to reduce the propagation loss in pulse energy before the two beams intersect. In fact, more energy will be delivered to the destination because the pulse tail erosion problem can be almost completely suppressed, especially when the intersection altitude is chosen to be near 50 km (1 torr pressure) where the breakdown threshold is minimum (so that the most effective ionization can be achieved). Such a low altitude can be used because the ionization patch will be tilted automatically to a large angle, (the average of the propagation angles of the two beams). Moreover, the ionization patch consists of a set of parallel plasma layers which are the consequence of interference between the fields of two beams. In the intersection region, field amplitudes varies periodically in space in the direction perpendicular to the plane bisecting the two beams. Using Bragg reflection to replace the conventional plasma cutoff reflection, the supplemental radar can then be operated in the much higher frequency satisfying the Bragg condition regardless of the lower cutoff frequency. Using this scheme, the location of the ionization layers can also be fixed easily. A schematic of the scheme is shown in Figure 3, which is further elaborated in Figure 4.

We have conducted a chamber experiment to examine the scientific feasibility of the second scheme. In order to achieve a meaningful simulation of the scheme, three major issues will be addressed by our chamber experiments. These include 1) the effectiveness of the plasma layers as a Bragg reflector, 2) the propagation of high power microwave pulse (HMP), and 3) the lifetime of the plasma. The chamber is a two foot plexiglass cube that is filled with dry air to a pressure corresponding to the simulated altitude. The microwave power is generated by a single magnetron tube

(OKH 1448) driven by a soft tube modulator. The magnetron delivers 1MW peak output power at a center frequency of 3.4GHz. The modulator uses a pulse forming network (PFN) having a pulse width which can be varied from 1.1 to 3.3μsec, with respective repetition rates from 60 to 20Hz. The microwave beams are fed into the cube, with parallel polarization directions, by two S-band microwave horns placed at right angles to adjacent sides. The plasma layers are then generated in the central region of the chamber where the two beams intersect. Shown in Figure 5 is a photo of the plasma layers which are manifested by the enhancement of the airglow from the corresponding locations. When one torr pressure is used, a maximum of eight layers can be generated, though only a few of them are shown in the photo. Shown in Figure 6a is the typical envelope of a 1.1 μsec pulse used for plasma generation. Using a focusing lens to localize the enhanced airglow, its temporal evolution between the two consecutive pulses is then recorded on the oscilloscope through a photomultiplier tube. A typical result is shown in Figure 6b. which manifests the growth and decay of the enhanced ionization. The decay time of about 7μsec is in agreement with the dissociative attachment loss time.

Without involving electrodes, determination of the breakdown threshold field, as a function of the air pressure, can be accomplished more accurately than the results of previous works. In order to achieve effective plasma generation, a set of more accurate data would be desirable for practical system design purposes. We have, hence, determined the Paschen breakdown curves for the cases of 1.1 and 3.3μsec pulses; the results are shown in Figure 7.

The microwave field is measured by a microwave probe which has been calibrated by a known waveguide field. The breakdown threshold is defined as that which is able to enhance minimum observable air glow which is monitored by the optical probe described above. Since a shorter pulse requires a larger ionization rate in order to generate the same amount of electrons, (which are proportional to the enhanced airglow flux), the threshold field is, therefore, accordingly increased. This tendency is clearly demonstrated in Figure 7. It shows that the breakdown threshold field for 1.1μsec pulse is always larger than that for a 3.3μsec pulse. The results also show that in both cases, the breakdown threshold field decreases with a decrease in air pressure and reaches a minimum in the 2 to 1 torr region where $\omega \cong \nu_c$; ω and ν_c are the microwave frequency and electron-neutral collision frequency respectively. With a further decrease in the pressure, the breakdown threshold field, E_c, increases again. The increase in E_c is also because the breakdown wave is in the pulse mode.

Since the ionization frequency is proportional to the pressure, lower pressure requires a larger field in order to maintain the ionization frequency. A simple theory based on above physical considerations is formulated. The dependence of $X = E_O/E_C$ on P (in torr) is given by the equation

$$X^{\alpha + 2/3} - X^{2/3}(P^2 + a)^{\alpha/2} - (b/w)P^{-1}(P^2 + a)^{(1/3 + \alpha/2)} = 0,$$

where $a = \omega^2/\nu_{co}^2$, $b = c/\nu_{ao}$, c is a constant parameter, ν_{c0} and ν_{aO} are the collision and attachment frequency, respectively, at 1 torr pressure, α is the power factor for the dependence of the ionization frequency on the field amplitude, E_C is the breakdown threshold for a CW wave, E_O is the breakdown threshold for the pulse, and w is the pulse width. The solid curves of Figure 7 are the theoretical results. (The dependance of the breakdown threshold field on the pressure is also manifested by a similar dependance of the degree of distortion of the tail portion of the transmitted pulse through the chamber). A series of snap shots demonstrating this behavior is presented in Figure 8. In the pressure regions pictured, the breakdown threshold is expected to be high, therefore, very little ionization can occur and, thus, the pulse can pass through the chamber almost without any loss (or distortion). However, as the pressure drops, the breakdown threshold also decreases before reaching the minimum, hence, more ionization occurs and also more distortion to the pulse. The distortion always starts from the tail of the pulse (ie tail erosion) because it takes finite time for plasma to build up and thus, maximum absorption of pulse energy by the generated electrons always appears in the tail of the pulse. Consequently, the leading edge of the pulse is usually not affected. Between 1 to 2 torr, the pulse appears to suffer maximum tail erosion and hence only very narrow leading edge pulses can pass through the chamber. The tail erosion becomes weak again for a further decrease in the pressure and can eventually be removed once the pressure becomes so low that the breakdown threshold power exceeds the peak power of the incident pulse.

We will now address the basic issues. The first issue to be considered is the effectiveness of the plasma layers as a Bragg reflector of radar pulses. The spatial distribution of the plasma layers is then measured with a three dimensional movable Langmuir probe (a double probe). As shown in Figure 9, the tip of the probe can be adjusted to move almost along a straight line across the plasma layers (which are visible). Figure 10 records the spatial dependance of the maximum probe current (since the breakdown wave is in pulse mode) for a fixed probe bias. In general, the electron density is proportional to the current and thus has similar

spatial distribution. The result shows that we have produced very sharp plasma layers with very good spatial periodicity. A Bragg scattering experiment is then prepared and will be described as follows.

Presented in Figure 11 is the block diagram of the experiment set up for a Bragg scattering study. In additional to the facility used for plasma generation (located to the left of the plexiglass chamber), a sweep microwave generator (4 - 8GHz) is used to generate a test wave which is incident into the chamber through a C-band horn. The incident angle of the test wave with respect to the normal of the plasma layers is 45 degrees. Hence, the S-band horn #2 located at right angle to the adjacent side can be used as the receiver of the Bragg scattered test wave. In order to separate the Bragg coherent reflection mechanism from the cutoff reflection mechanism, the test wave is swept in the frequency range much higher than the plasma cutoff frequency. Consequently, the test wave will be received by the S-band horn #1 even during the presence of the plasma. The amplitude of this signal is reduced by using a directional coupler; nevertheless, it represents a large noise to the real scattered signal. To resolve this problem, a standard noise cancellation technique is used. The microwave components used for noise cancellation are shown in the diagram. A HP spectrum analyzer (8569B) is used for recording the scattered signal. Now, the question is how do we know the noise signal received by horn #1 is not affected by the presence of the plasma layers. This is examined by reversing the directional coupler connected to horn #2. Since the scattered signal is expected to be very weak (the frequency range of the test wave is far from satisfying the Bragg condition), and since the direction of the directional coupler is unfavorable to the scattered signal, the output of the directional coupler at the test wave frequency can be considered to solely come from the signal received by horn #1. The results indicate that the plasma has no detectable effect at all. In other words, the output of the directional coupler is completely insensitive to the presents of the plasma layers. This is also understandable because the test wave frequency is much higher than the plasma cutoff frequency.

Presented in Figure 12 are the outputs of the spectrum analyzer for two cases. Figure 12(a) shows that no signal is received when there is no plasma. However, an appreciable scattered signal is detected as shown in Figure 12(b) whenever the plasma layers are produced. A clear signature of Bragg scattering has been demonstrated. Next question is that how does the experimental result compare with the theory. A simple plasma model shown in Fig. 13 is used for theoretical formulation. In terms of this plasma distribution, the dielectric function of the

medium at the test wave frequency is given by

$$\varepsilon(z) = 1-[\frac{\omega_{po}^2}{2\omega_o(\omega_o + i\nu_c)}] [P_{L/2}(z-L/2)(1 - \cos 2\pi\frac{z}{d})] \quad (1)$$

where $P_{L/2}$ is a rectangular pulse of width L and amplitude one; d is the separation between two adjacent plasma layers and L=Nd for N layers; ω_{po}^2 is the maximum electron plasma frequency, and ω_o and ν_c are the wave frequency and electron-neutral collision frequency respectively.

Assuming that the incident test wave is TE mode, the total wave electric field can then be expressed as

$$\vec{E}_t = \hat{y}\, \varepsilon_t(z)e^{i(k_{ox}x - \omega_o t)}. \quad (2)$$

Substitute (2) into the wave equation, which is then reduced to be

$$\frac{\partial^2}{\partial z^2}\varepsilon_t(z) = (k_{ox}^2 x - \omega_o^2/c^2)\, \varepsilon_t(z) + \frac{1}{2}[\frac{\omega_o\omega_{po}^2}{(\omega_o + i\nu_c)c^2}]P_{L/2}(z - L/2)(1-\cos 2\pi\frac{z}{d})\varepsilon_t(z) \quad (3)$$

Using perturbation expansion, along with Fourier and inverse Fourier transforms, the reflected wave amplitude is obtained after a contour integration. The reflection coefficients of the wave intensity is then obtained analytically to be

$$R = \left|\frac{\varepsilon_r}{\varepsilon_{in}}\right|^2 = k_d^4[\frac{\omega_o^2\omega_{po}^4}{(\omega_o^2 + \nu_c^2)c^4}] \frac{(\sin k_{oz}L)^2}{[4k_{oz}^2(k_{oz}^2 - k_d^2)]^2}, \quad (4)$$

where $k_d = 2\pi/d$.

This reflection scattering coefficient of wave intensity is then plotted as a function of the test wave frequency in Figure 14. By sweeping the test wave frequency, such a dependance is also determined experimentally in a relatively small frequency range and presented in the same Figure 14 for comparison. Besides an uncalibrated absolute magnitude, the two functional dependences are shown to agree with each other very well. Since the frequency of the test wave which satisfies the Bragg condition, $2d\sin\vartheta = \lambda_d$ for the current experimental arrangement, is equal to the frequency of the breakdown pulses, which then represent a very strong noise to prevent any meaningful test of Bragg scattering at this frequency, and in fact, also in the neighborhood frequency region. Although, the optimum frequency region for Bragg scattering is not examined, nevertheless the consistency between theoretical predictions and experimental results may lead us to conclude, based on the maximum theoretical reflection coefficient, that plasma layers can indeed be an effective Bragg reflector, especially when the number of layers is increased to the order of 50 that will be generated in the upper atmosphere.

We next consider the subject concerning the propagation of high power

microwaves pulses through the atmosphere. Two goals are aimed. One is to determine the parametric range lending to maximum energy transfer by the pulse after a prescribed distance of propagation; and the other is to determine means of maximizing the electron density generated by the pulses at the destined location. In order to achieve these goals, we first identify experimentally, the mechanisms which cause tail erosion of the pulses. Tail erosion is a common phenomenon appearing in the propagation of high power microwave pulses. This occurs because ionization by the wave field gives rises to a space-time dependant plasma which attenuates the tail of the pulse but does not affect the leading edge because of the finite time for the plasma to build up. This phenomenon is demonstrated by the snap shots presented in Figure 15, where 1.1μsec pulses, with four consecutively increasing amplitudes, are transmitted into the chamber from one side and received, as shown in the Figure, from the opposite side. The first pulse has amplitude below the breakdown threshold, and hence, nothing is expected to happen. Consequently, the received pulse shape is undistorted from that of the transmitted pulse. Once the amplitude exceeds the breakdown threshold, more tail erosion occurred to the larger amplitude pulses, as is observed by the subsequent three snap shots. This is because the increase of the ionization rate with field amplitude allows more electrons, which attenuate the pulse, to build up. Now, let's focus on the last two pictures. Pulses have been eroded strongly in both cases. However, a clear distinction between the two cases is noticed. In one case corresponding to the third picture, the erosion to the tail of the pulse is not complete. In other words, the received pulse width extends to the original width. In the other case, a large portion of the tail of the pulse is more or less eroded completely during the finite pulse length. However, it is a different mechanism responsible for the second case. The ionization frequency becomes so large in the second case that the electron density reached the cutoff density before the whole pulse passes through. The overdense plasma screen reflects the remaining portion of the pulse and causes even more severe tail erosion. In summary, two mechanisms responsible for the tail erosion are identified. One is due to attenuation by the self-generated underdense plasma. The other one is caused through reflection by the self-generated overdense plasma screen. These two processes are also verified by the reflected power level measured for each case. As shown in Figure 16, the snap shots presented on the RHS of the Figure represent the reflected pulse shape corresponding to each received pulse presented on its left. As shown by the last set of pictures, strong reflection and complete erosion are observed

consistently.

This study indicates that an increase of pulse amplitude may not help to increase the energy transfer by the pulse. This is because the two tail erosion mechanisms degrade the energy transfer. One way to solve the problem is to lower the amplitude of the pulse in order to minimize the propagation loss, and to use several low amplitude pulses to deliver the required field strength to the intersection region of the pulses. Usually, two pulsed beams are adequate. We, therefore, propose to use two crossed beams for plasma generation purposes. We also chose the 47km height as the ionization altitude for the reason that the breakdown threshold field is minimum around the region of this altitude. The remaining question is that of optimum parameters for the pulses in order to achieve effective ionization.

Unfortunately, this question can not be answered by the chamber experiments. A numerical code of pulse propagation has been set up to address this question. Shown in Figure 17 is a schematic diagram of the two beam scheme where the propagation angle of each beam and their relative locations are indicated. Two 550nsec pulses with carrier frequency 3.6GHz are used. Each pulse has its intensity 2.15 times the value of the breakdown threshold intensity at 1 torr pressure. It is found that such pulses experience very little propagation loss and can generate plasma layers in the intersection region with maximum density larger than $10^{11}cm^{-3}$. The generated density profile along one beam trajectory as a function of the altitude is presented in Figure 18. The feasibility of the two intersecting beam scheme for the generation of plasma layers is clearly demonstrated. We next determine the optimum parameters of the pulses for the most effective ionization. The relation between the pulse energy and width is then evaluated numerically, where the pulse energy is defined to be the minimum required energy carried initially by each pulse so that the maximum plasma density in the intersecting region can reach the cutoff density. As shown in Figure 19, the required pulse energy is minimized for a 200nsec pulse, where $\varepsilon_{1\mu s}$ represents the required pulse energy for a 1μsec pulse. Converting the pulse width, w, to the field amplitude E_o, the dependence of $\varepsilon/\varepsilon_{1\mu s}$ on $E_o/E_{1\mu s}$ is presented in Figure 20. Such dependences can be realized by the strong dependence of the ionization frequency ν_i on the field amplitude E_o. Shorter pulses require larger ionization frequency which, however, requires only a slight increase of E_o.

Finally, we have to examine the lifetime of the plasma. We use the optical

probe to monitor the decay of the enhanced airglow, which is in turn , proportional to the decay of the plasma density. Using two 1.1μsec pulses for plasma generation in 1 torr air, it is shown in Figure 21a that the plasma decay is very fast during the first 10μsec after the microwave is off. The decay time is about 7μsec, consistent with the dissociative attachment loss time. However, the decay rate becomes very slow after 20μsec when the density drops from the peak 1.6×10^{11} cm^{-3} to about $5\times10^{9}cm^{-3}$. It takes about 80μsec for density decay from 5×10^{9} to about $7.5\times10^{8}cm^{-3}$. As shown in Figure 21b, $n_e \propto 1/(t-t_a)$, it is a clear indication that the loss is mainly contributed by the re-combination process. In other words, the electron loss through attachment is balanced out by the electron gain through detachment, and the net loss is through the re-combination. This study shows that the attachment loss process can be overcome if dense plasma can be generated initially so that the attachment process is saturated (by the balance with the detachment process) by the time electron density is reduced to the desired level. Therefore, the working electrons can have desirable long lifetime, which, thus, reduces the required maintenance power.

In summary, a Chamber experiment has been performed to study the feasibility of using two intersecting beams for plasma generation in the upper atmosphere as a radar reflector. Three critical issues consisting of 1) reflectivity of the generated plasma layers, 2) propagation of high power microwave pulses, and 3) lifetime of the plasma have been addressed. The results of the experiments show that there seems no obvious obstacle in the way to impede the scheme; therefore, what we next have to do is to make a conceptual design of the scheme, and give a scientific, technical, and economic assessment of the scheme.

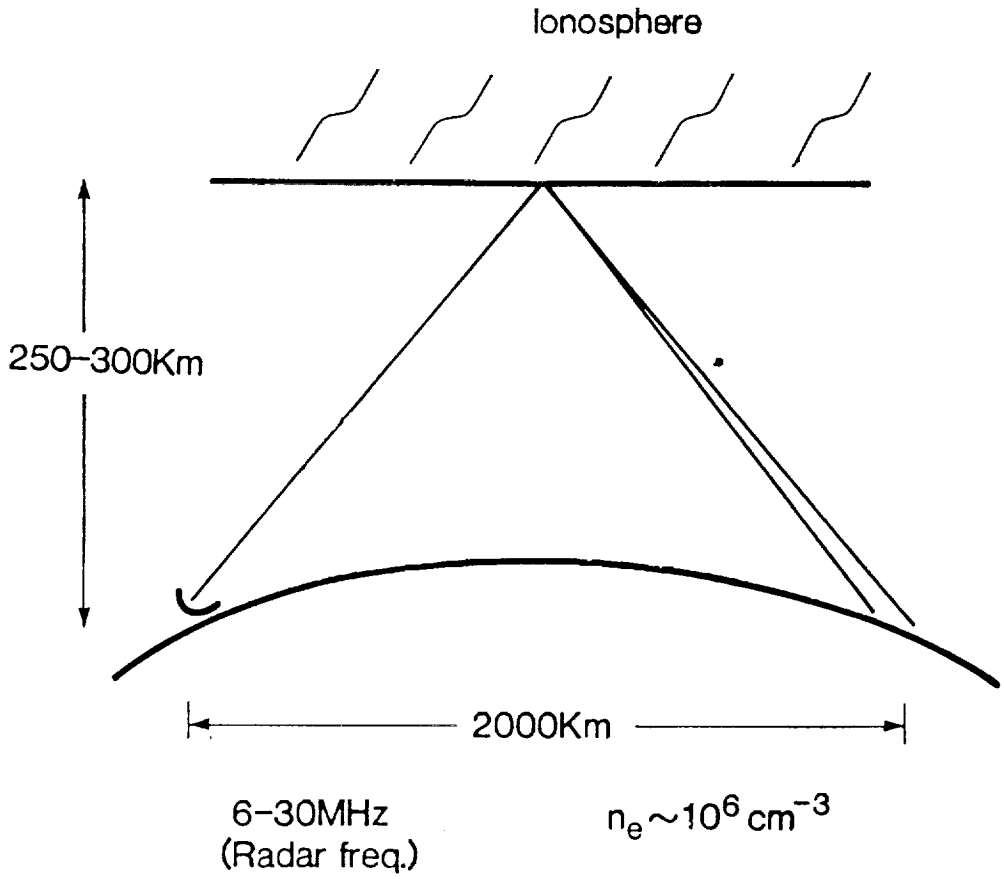

Figure 1. OTH Radar using ionosphere as a mirror

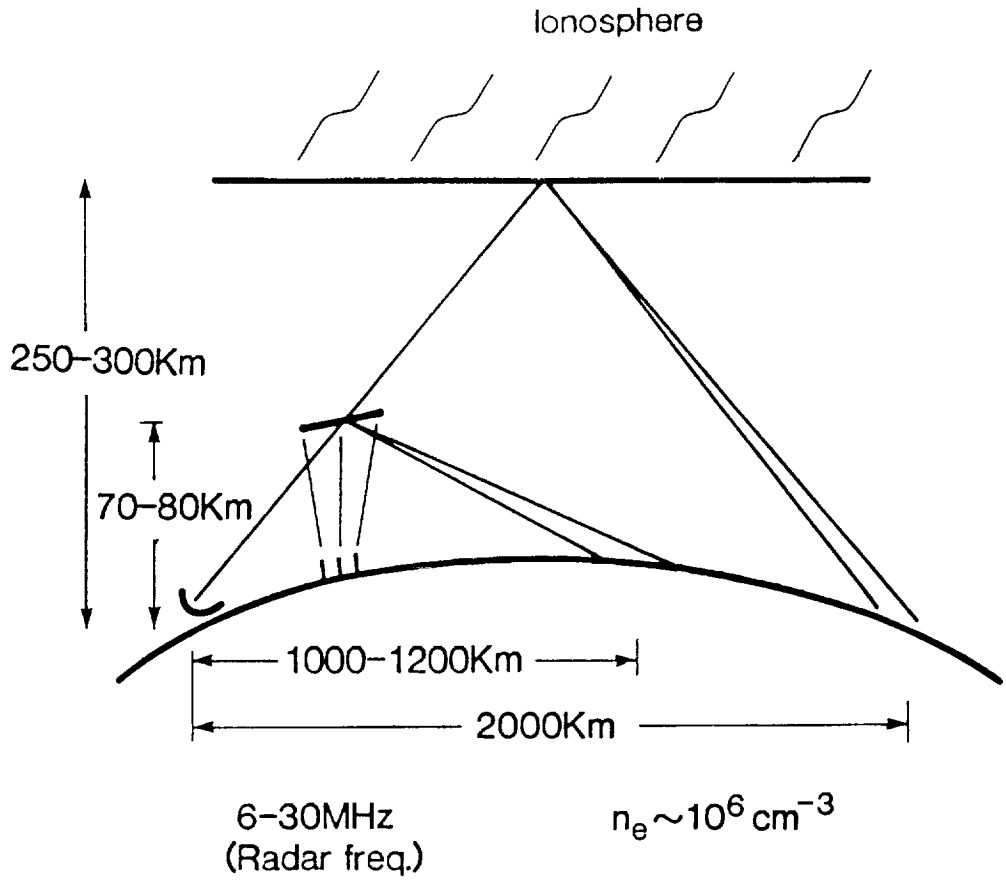

Figure 2. OTH Radar using artificial plasma patches as a mirror

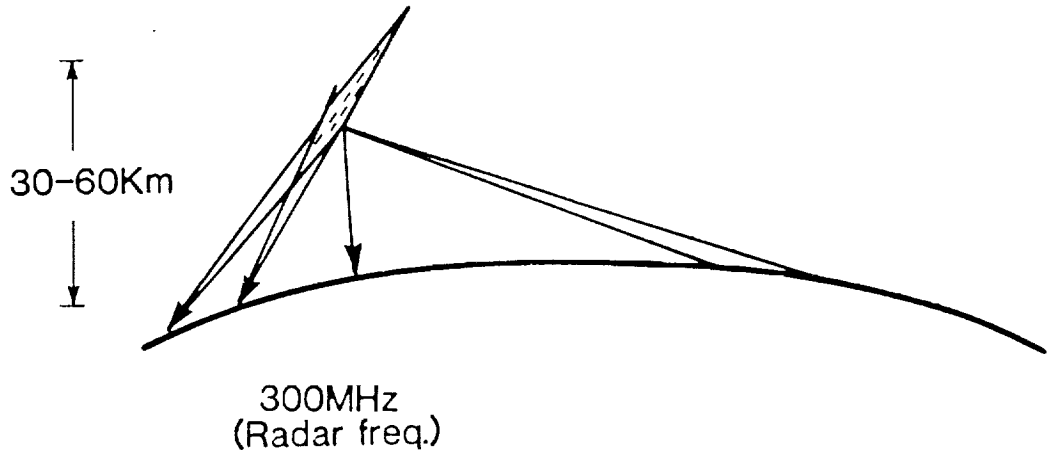

Figure 3. Two crossed beam scheme

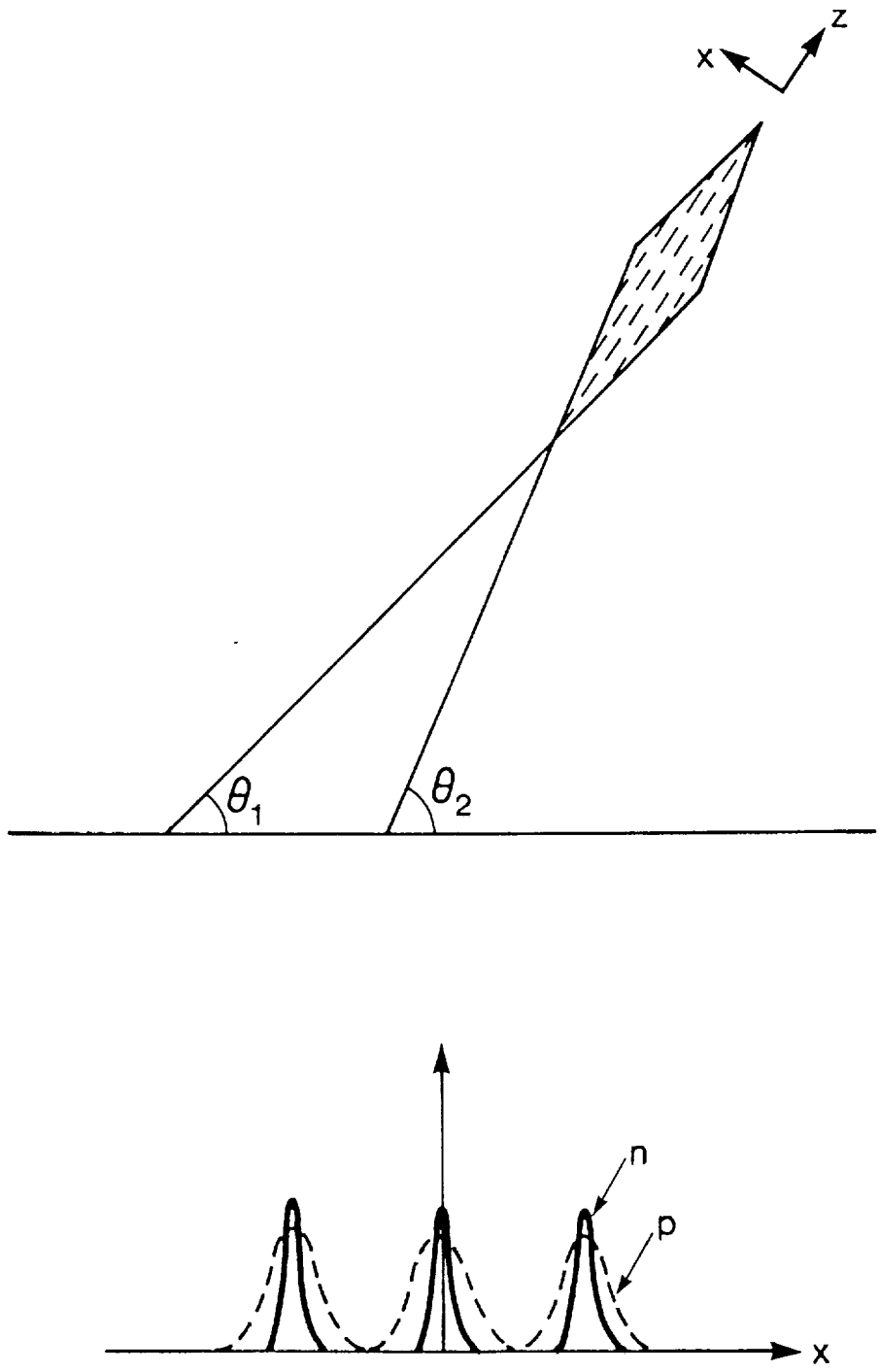

Figure 4. Illustration of two intersecting beams and plasma layers

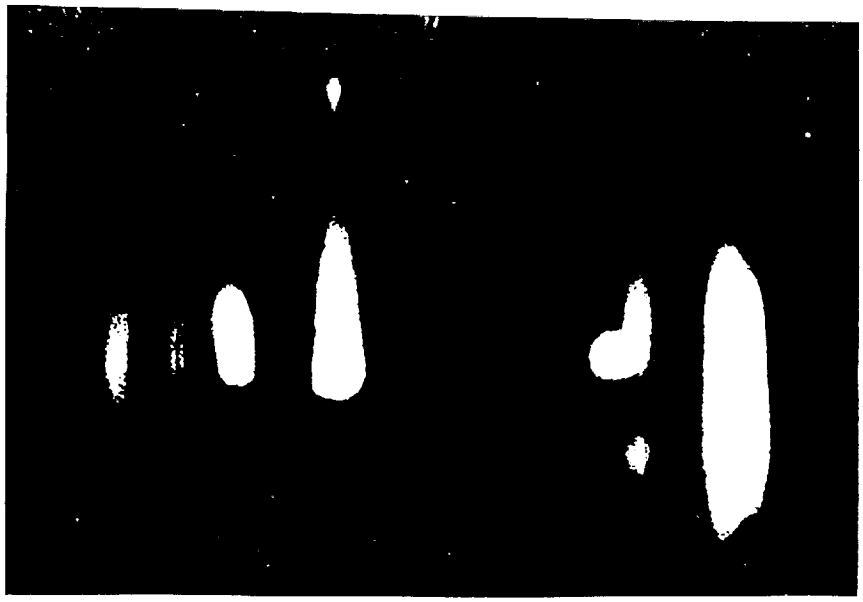

Fig. 5 Plasma layers produced in the chamber

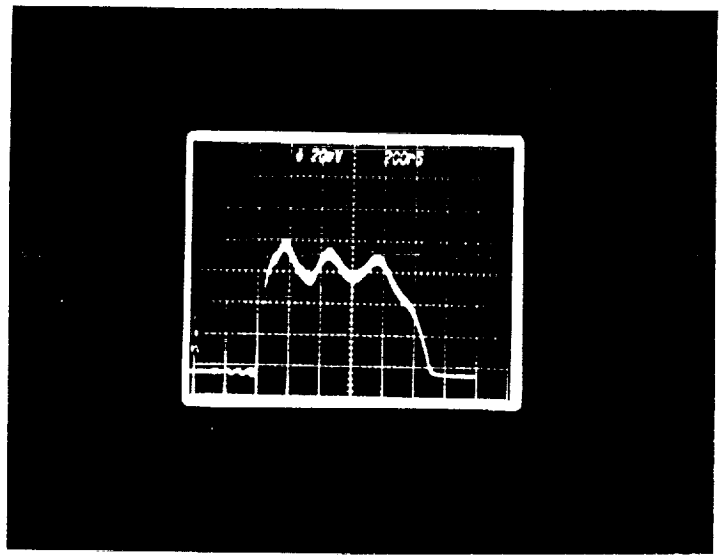

Fig. 6 (a) Envelope of the 1.1 microsecond microwave pulse

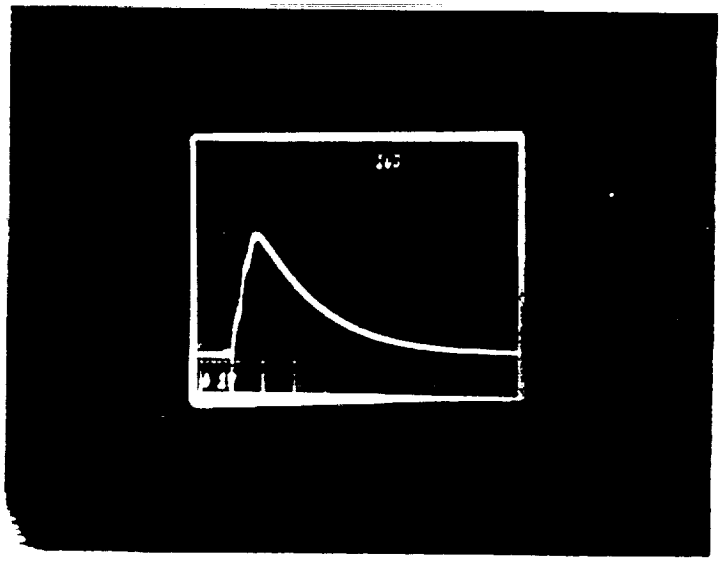

Fig. 6 (b) Growth and decay of plasma glow measured by an optical probe

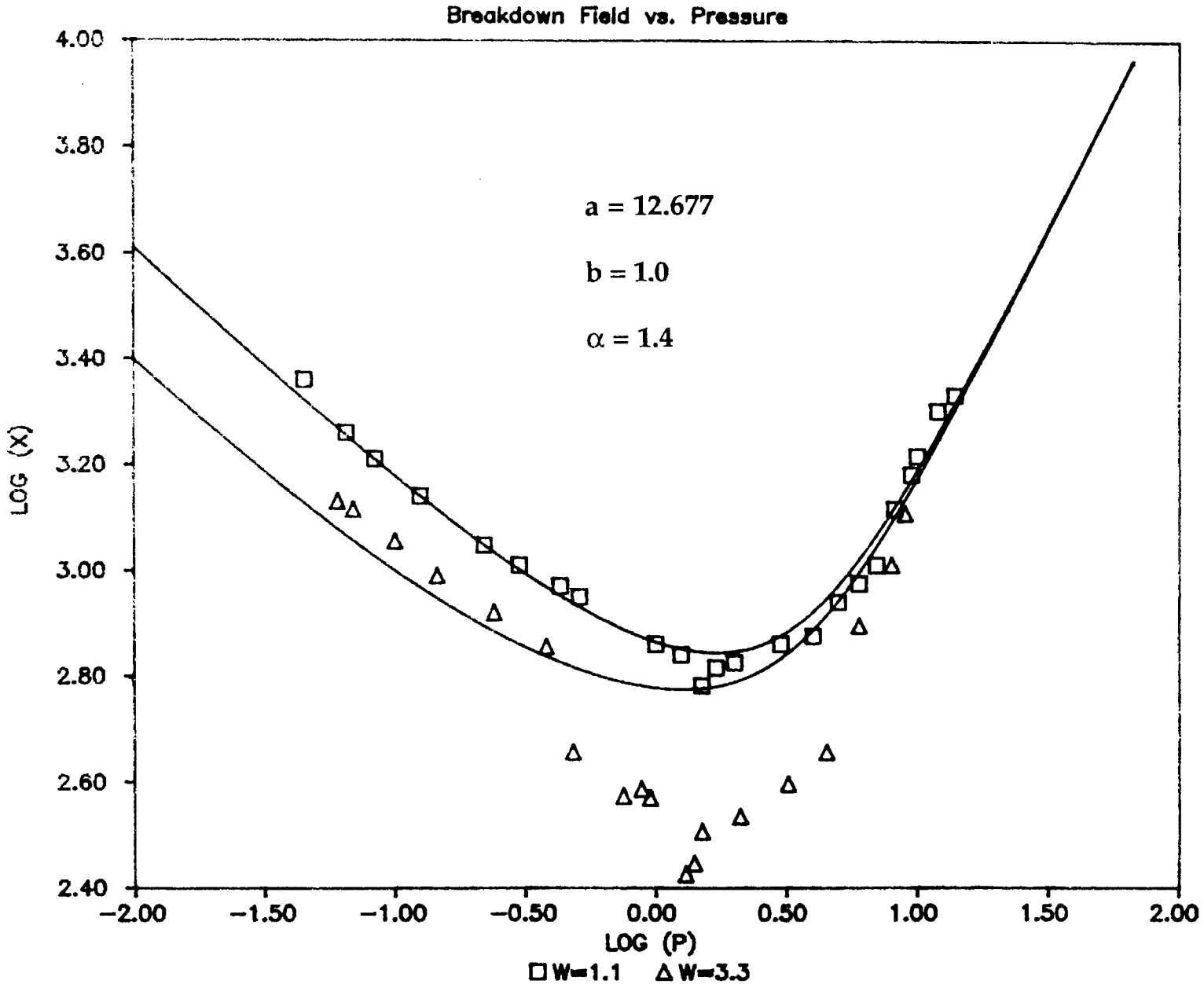

Figure 7. Air Breakdown threshold

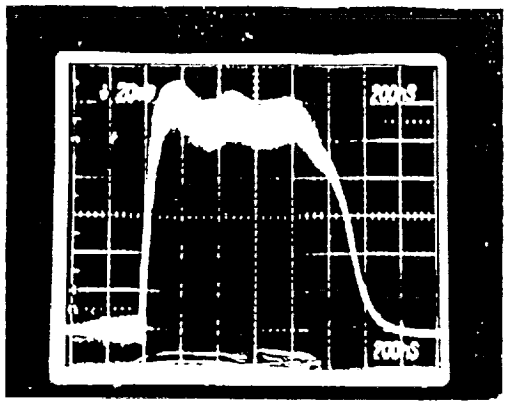

P=8 torr

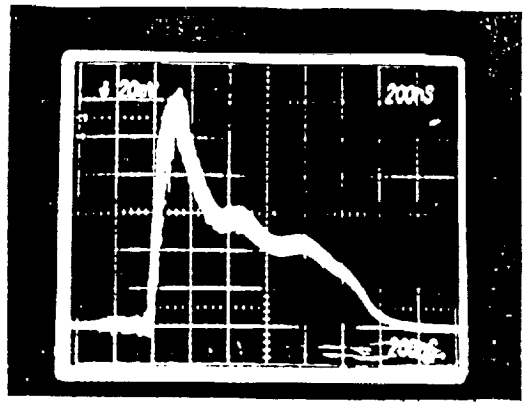

P=4 torr

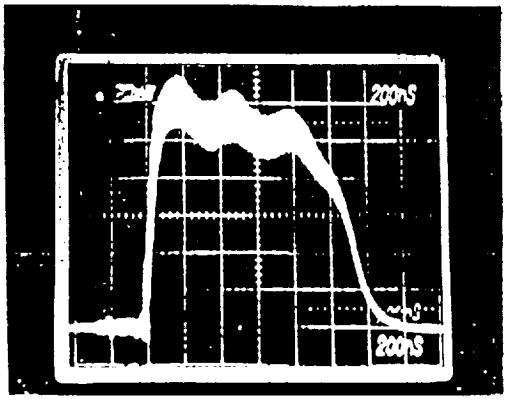

P=6 torr

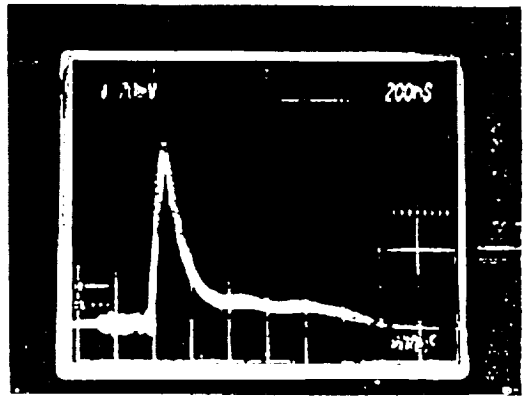

P=2 torr

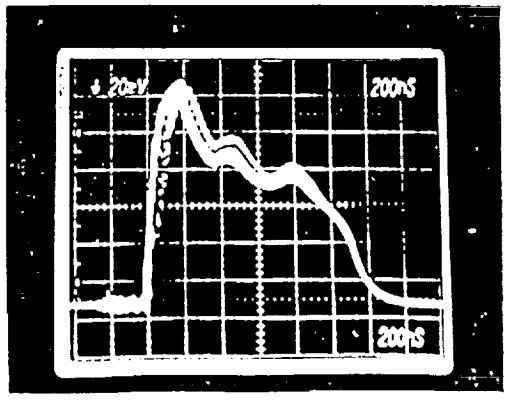

P=5 torr

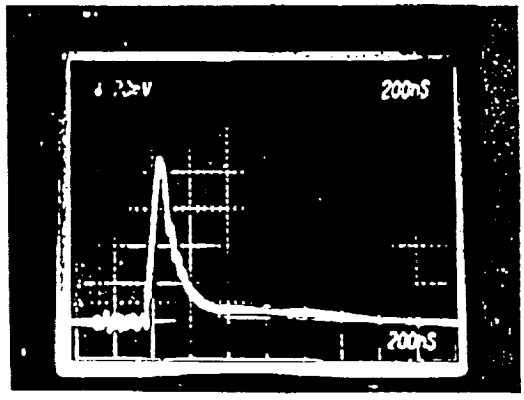

P=1 torr

Fig. 8

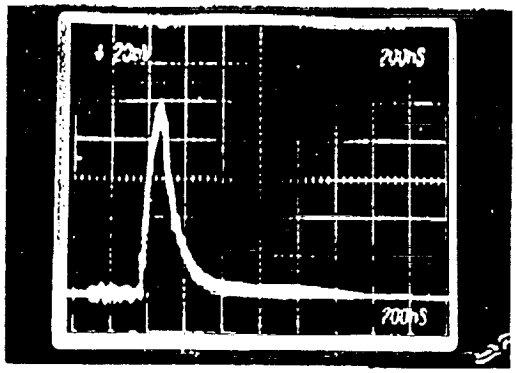

P=0.45 torr

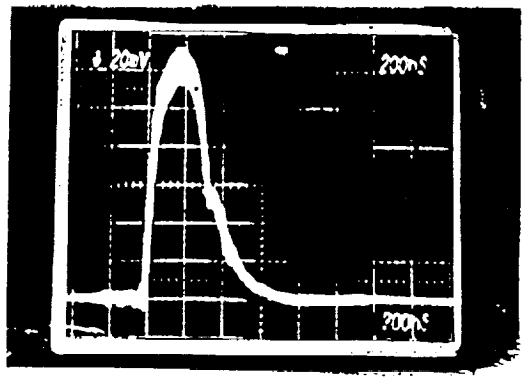

P=0.07 torr

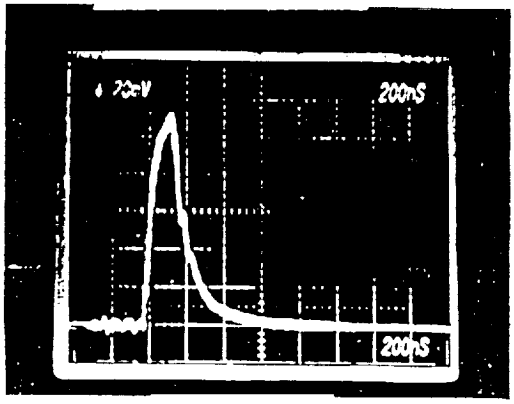

P=0.2torr

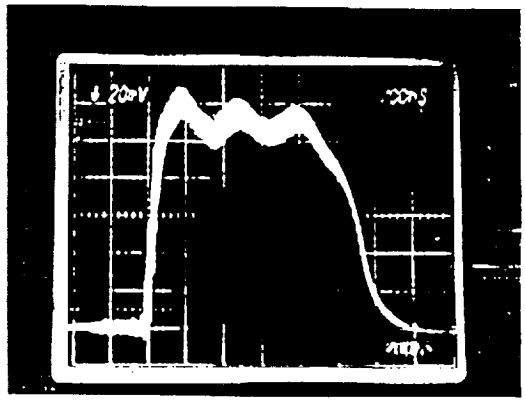

P=0.05 torr

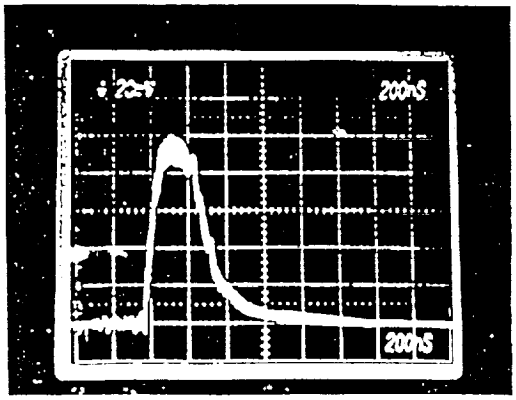

P=0.1 torr

Fig. 8 Microwave pluse transmission through air at different pressure

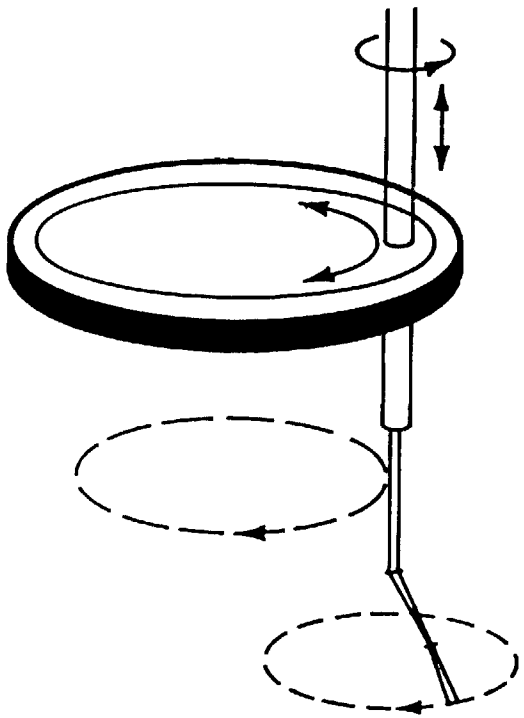

Three Dimensional movable probe.

Figure 9.

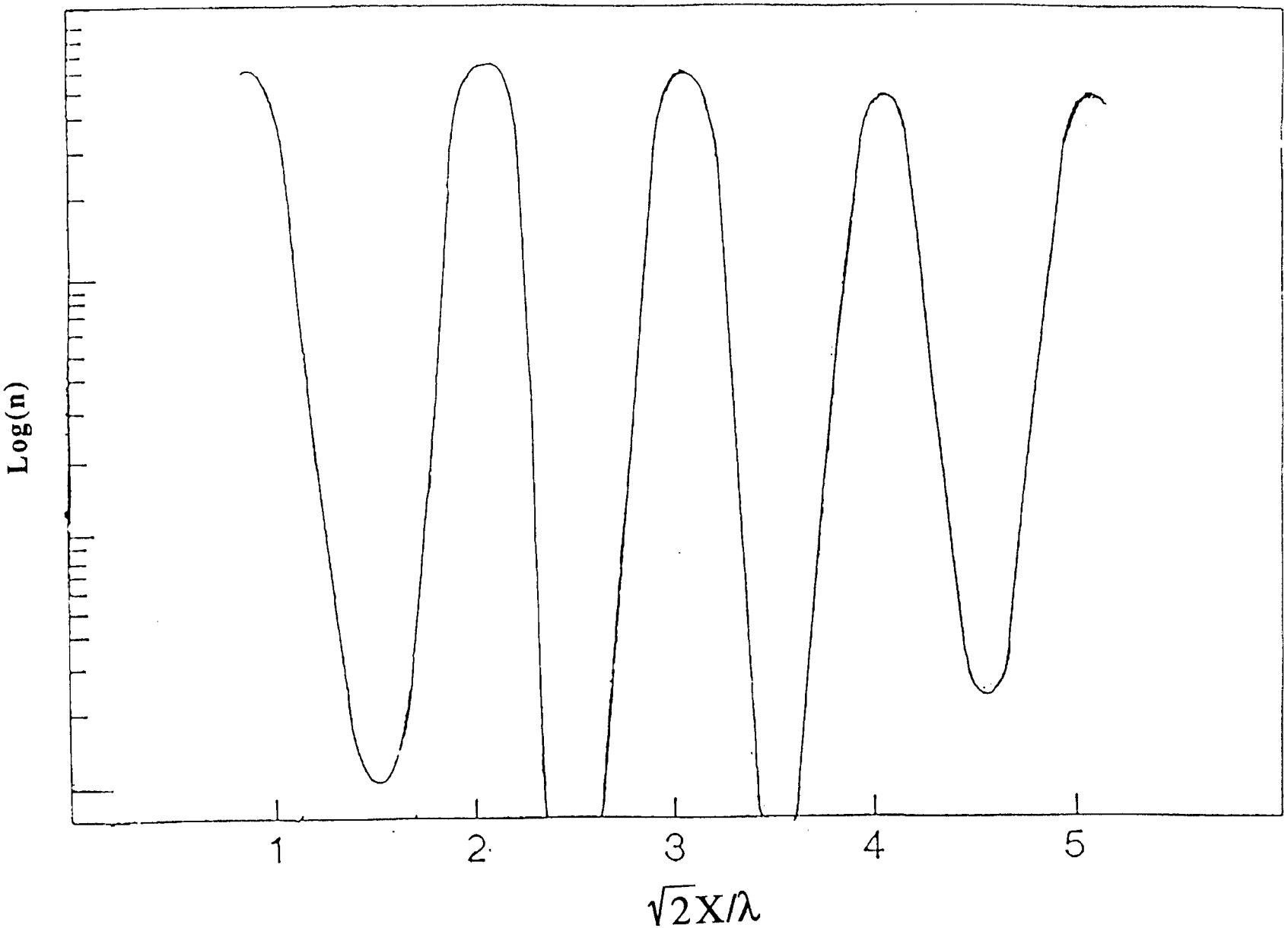

Fig. 10 Probe measurement of the density distribution along the direction transverse to the plasma layers

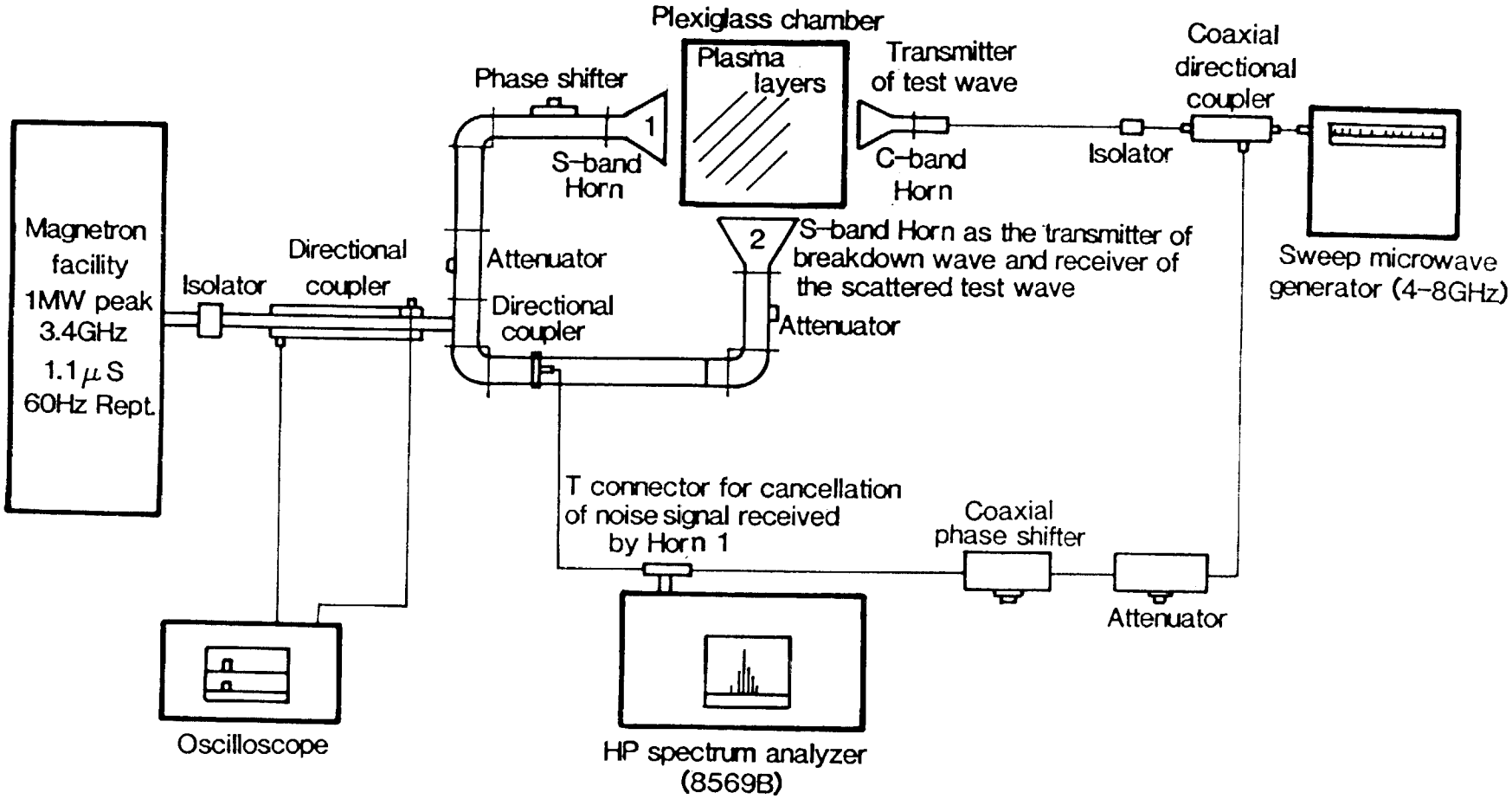

Figure 11. Microwave Bragg scattering experimental set-up

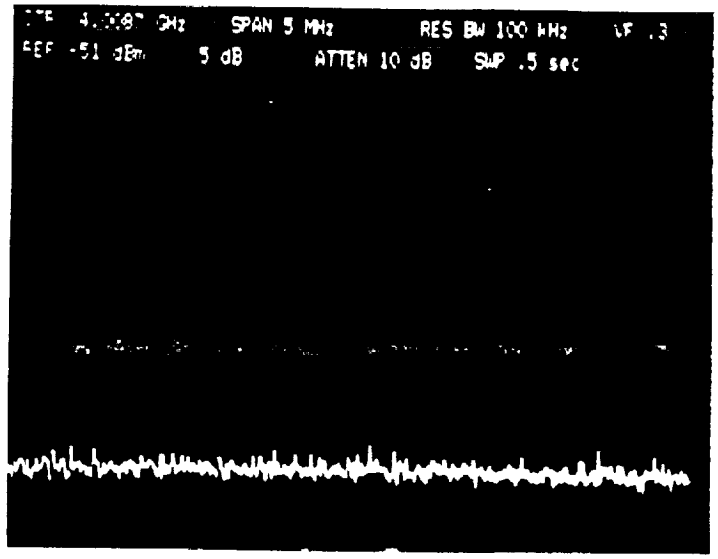

(a)

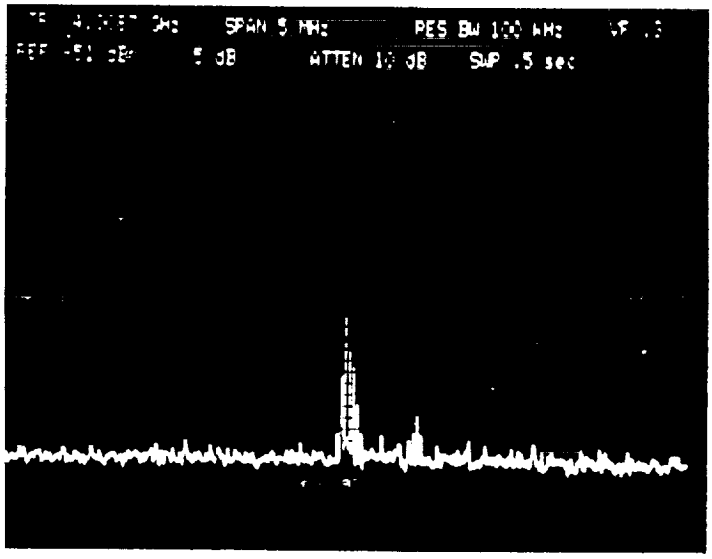

(b)

Fig. 12 Spectrum analyzer CRT display
(a) No signal is receved when plasma is off
(b) Spectrum of scattered test wave when pasma layers are pesent

Bragg Scattering:

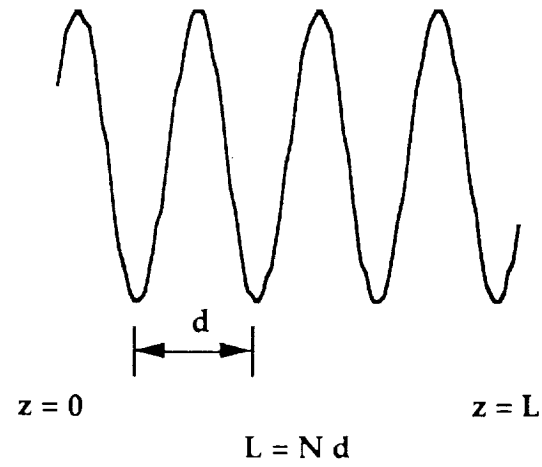

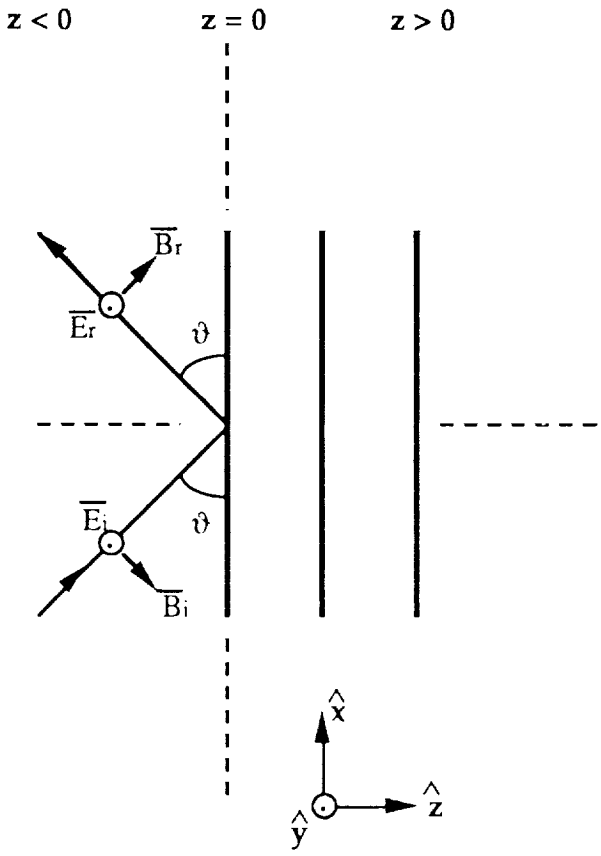

Figure 13. Model of wave scattering from plasma layers

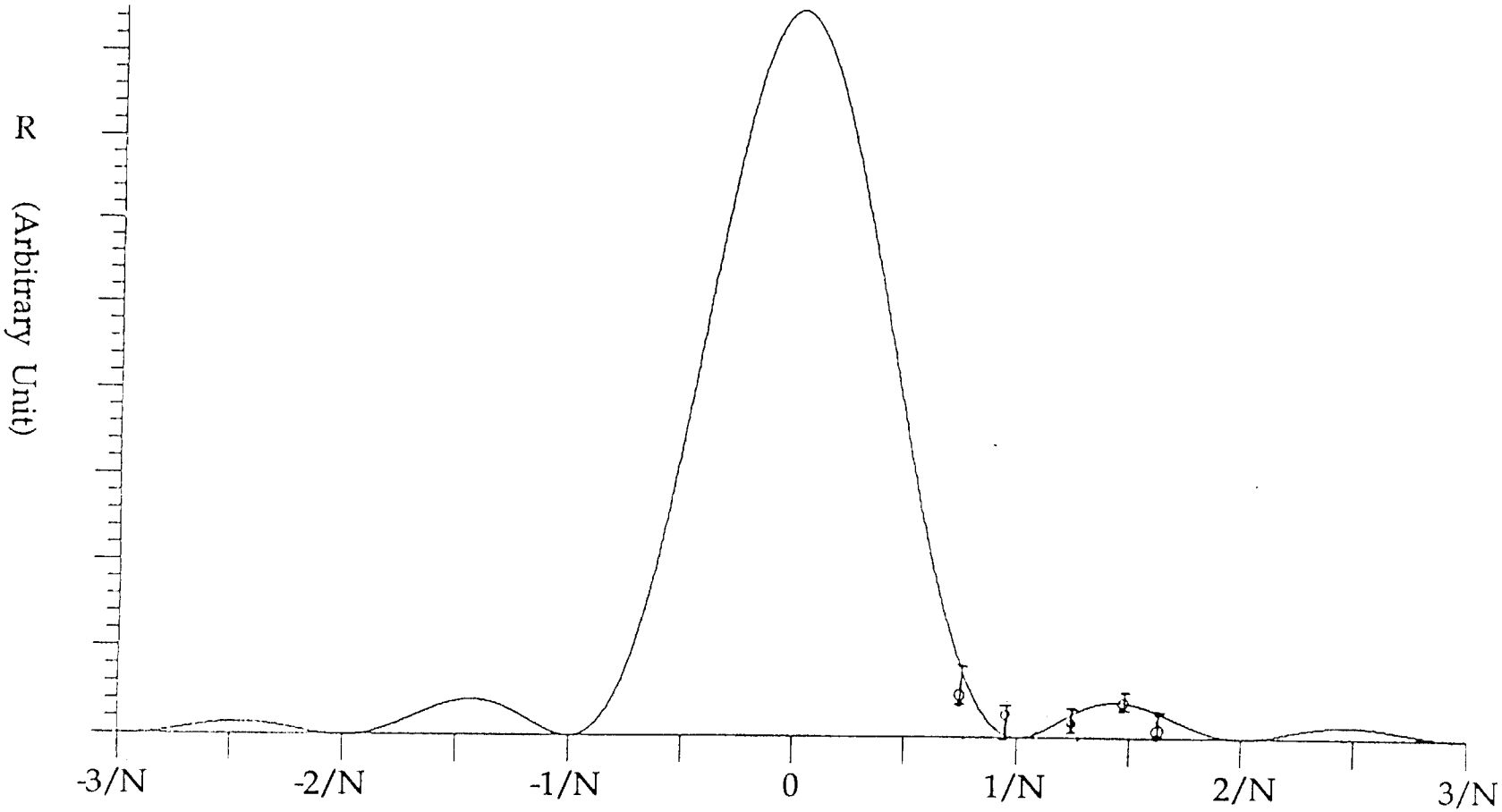

Fig. 14 Reflectivity of plasma layers predicted by theory
& Experimental result

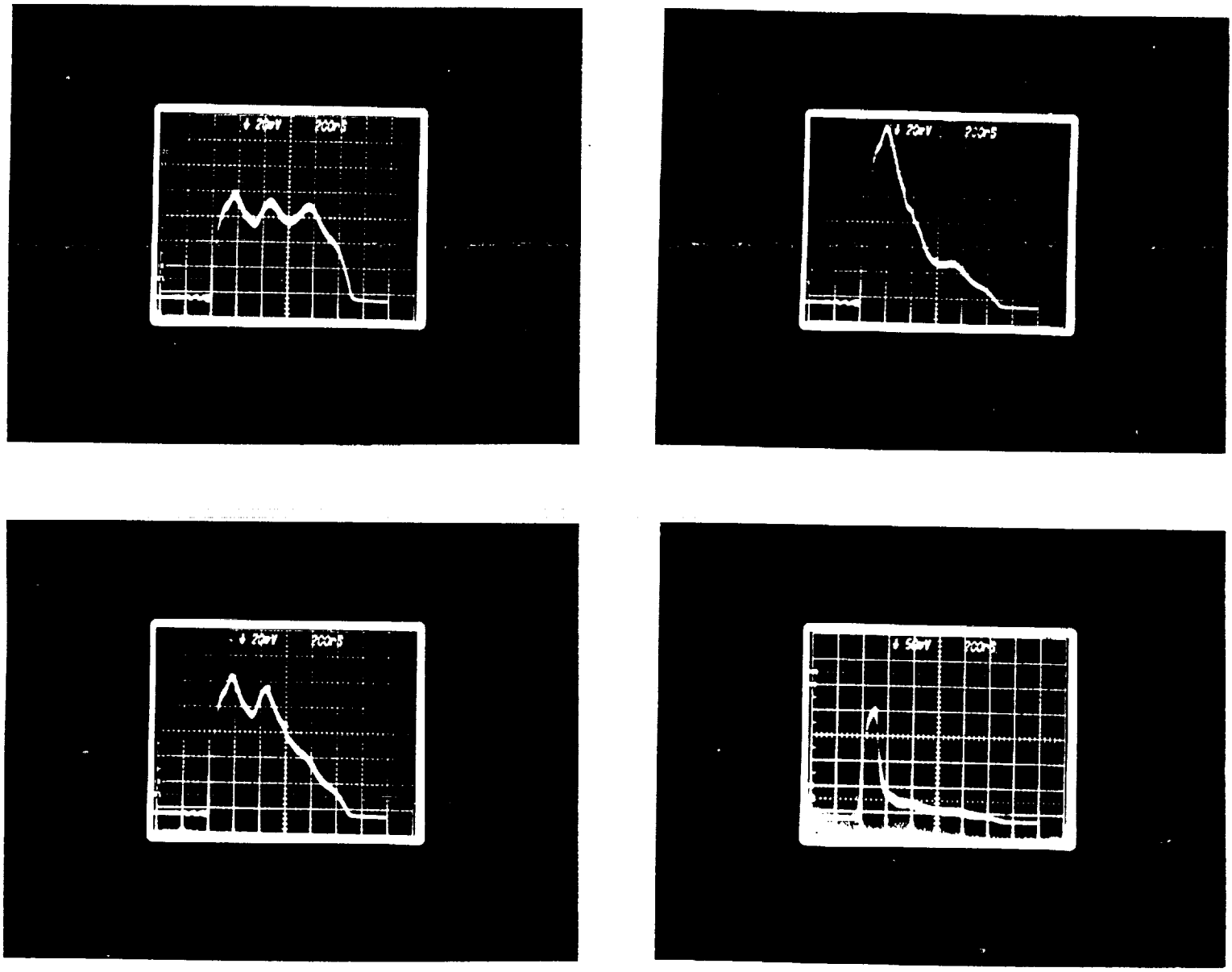

Fig. 15 Tail errosion of microwave pulse

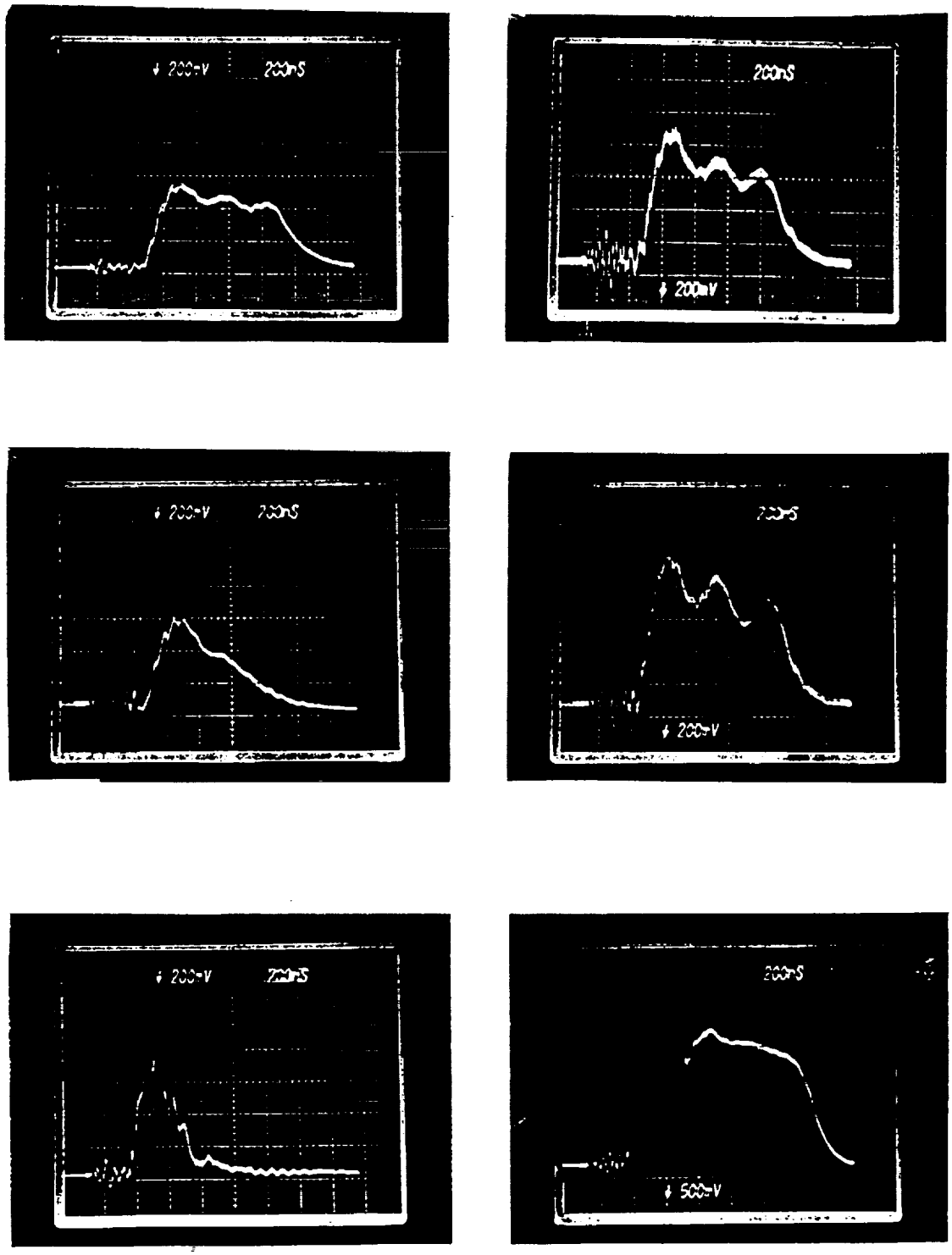

Fig. 16 Transmitted pulses and corresponding reflected pulses

$\vartheta_1 = 40^o$

$\vartheta_2 = 60^o$

D = 29km

d = 0.96m

Microwave: f_o = 3.6GHz

Radar Freq.: f_b = 200MHz

Range: 1200km

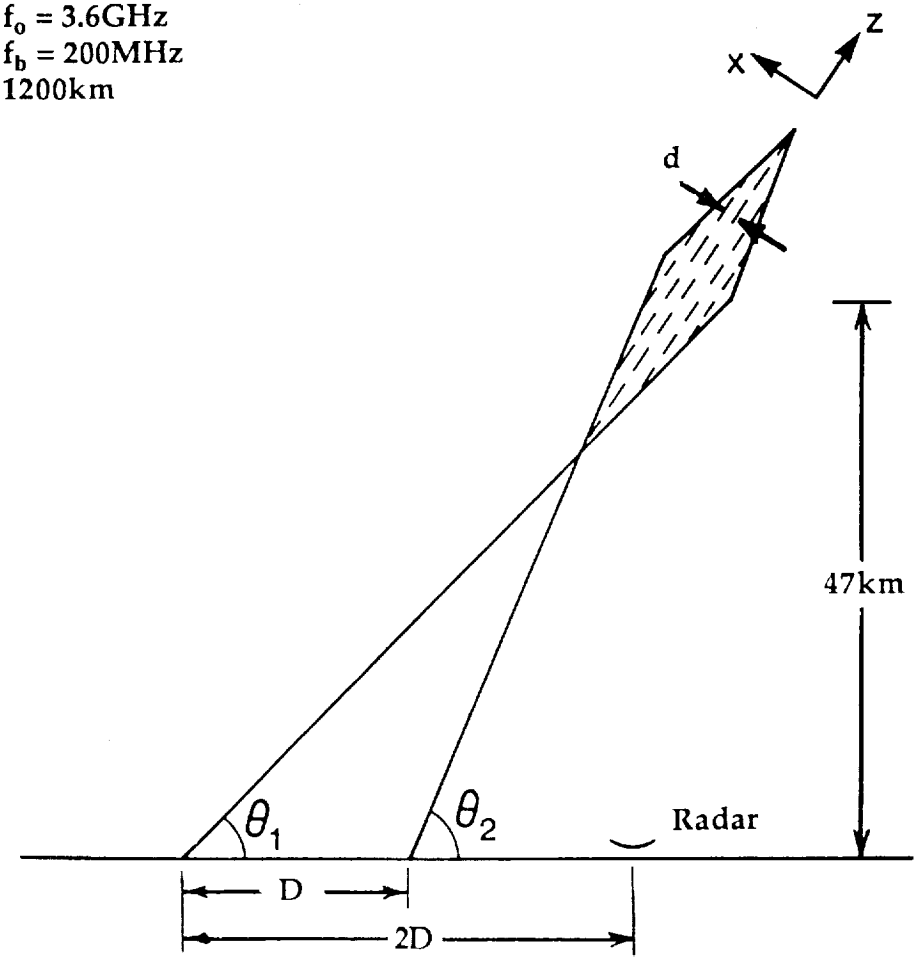

Figure 17. Diagram of two beam scheme with parameters chosen in computer simulation

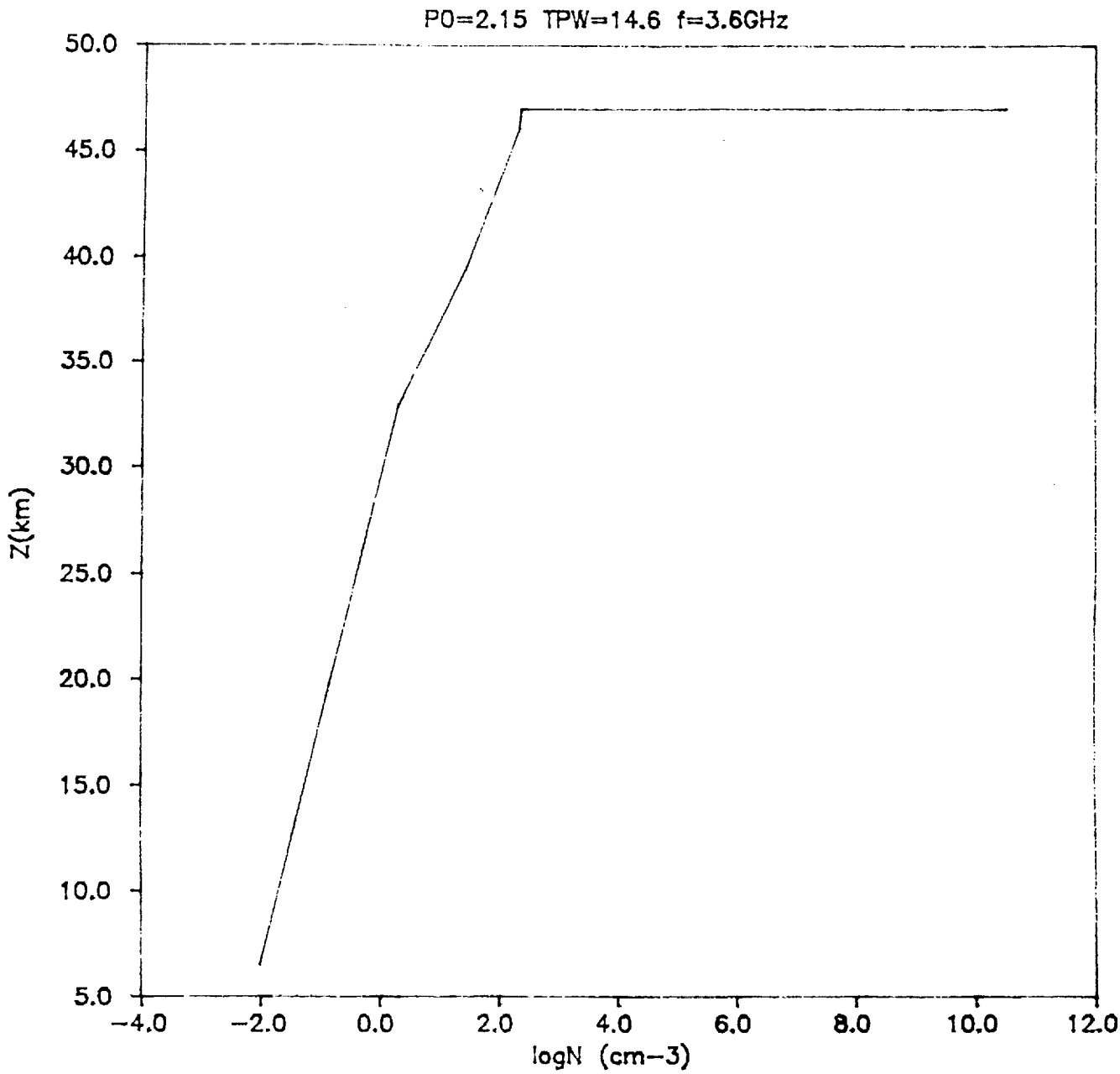

Fig. 18 Electron density profile along one beam trojectory

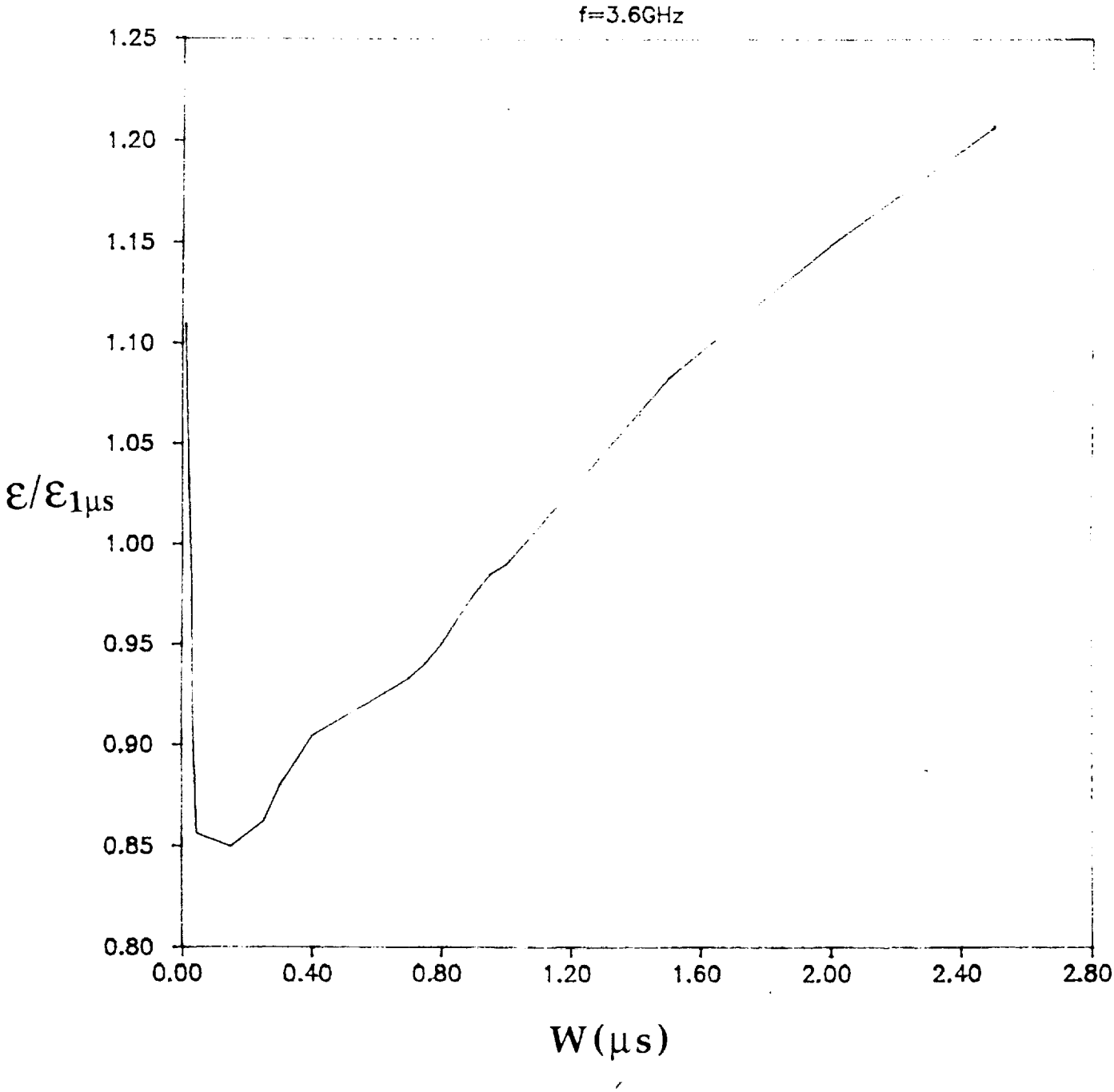

Fig. 19 Minimum pulse energy required as a function of pulse width

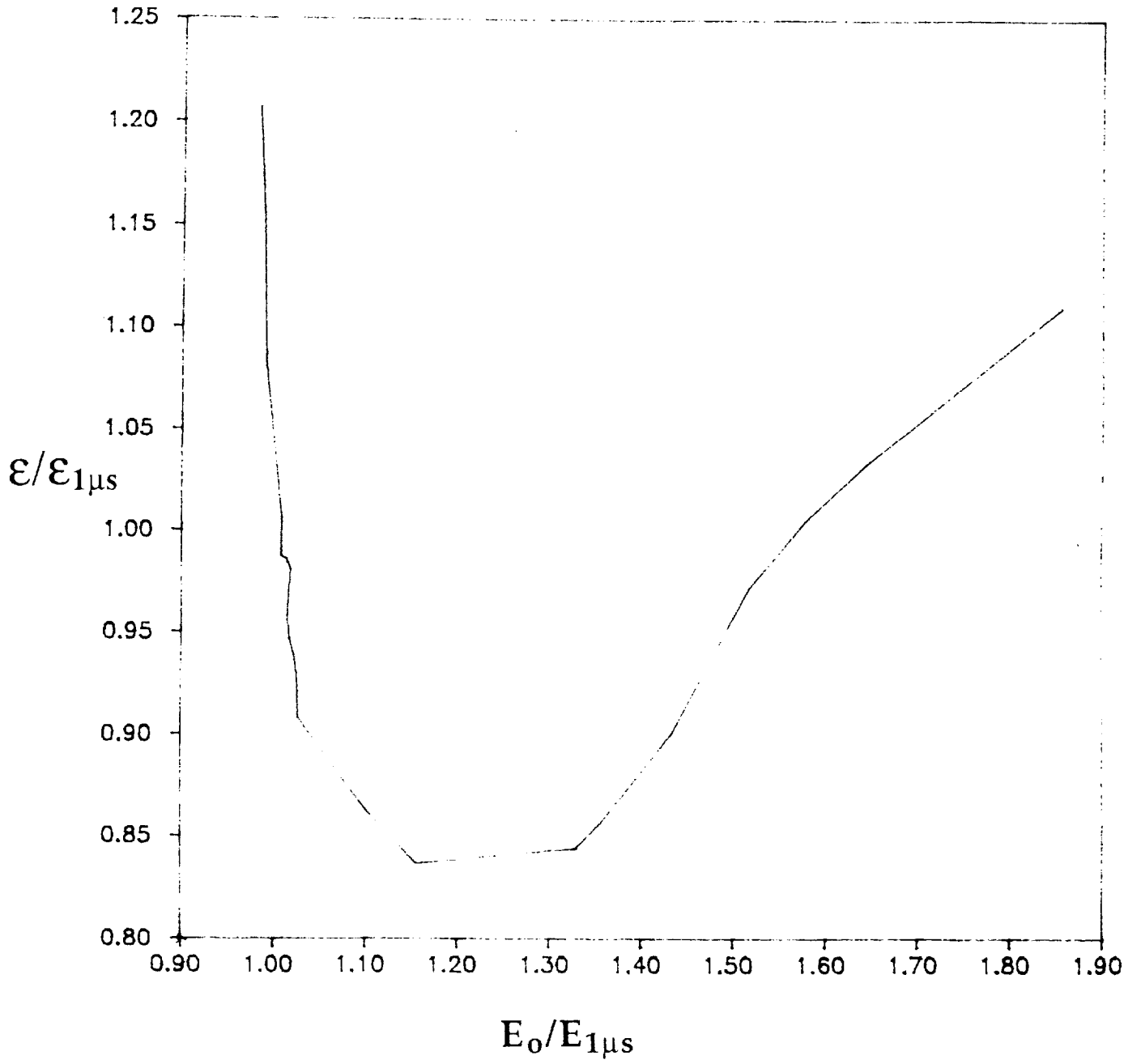

Fig. 20 Pulse energy required as a funtion electrical field intensity

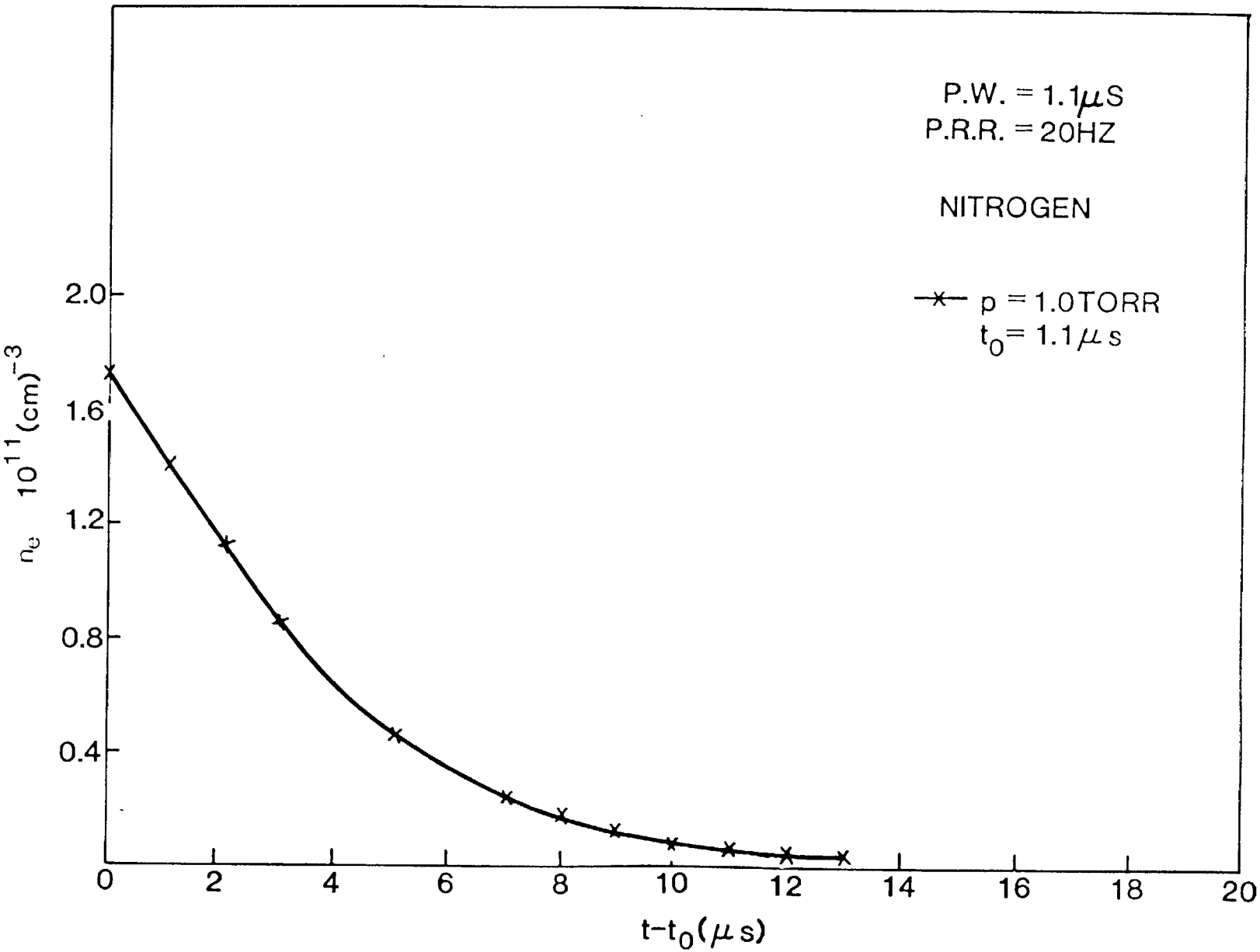

Figure 21(a). Plasma decay during the first 10μsec after the microwave pulse

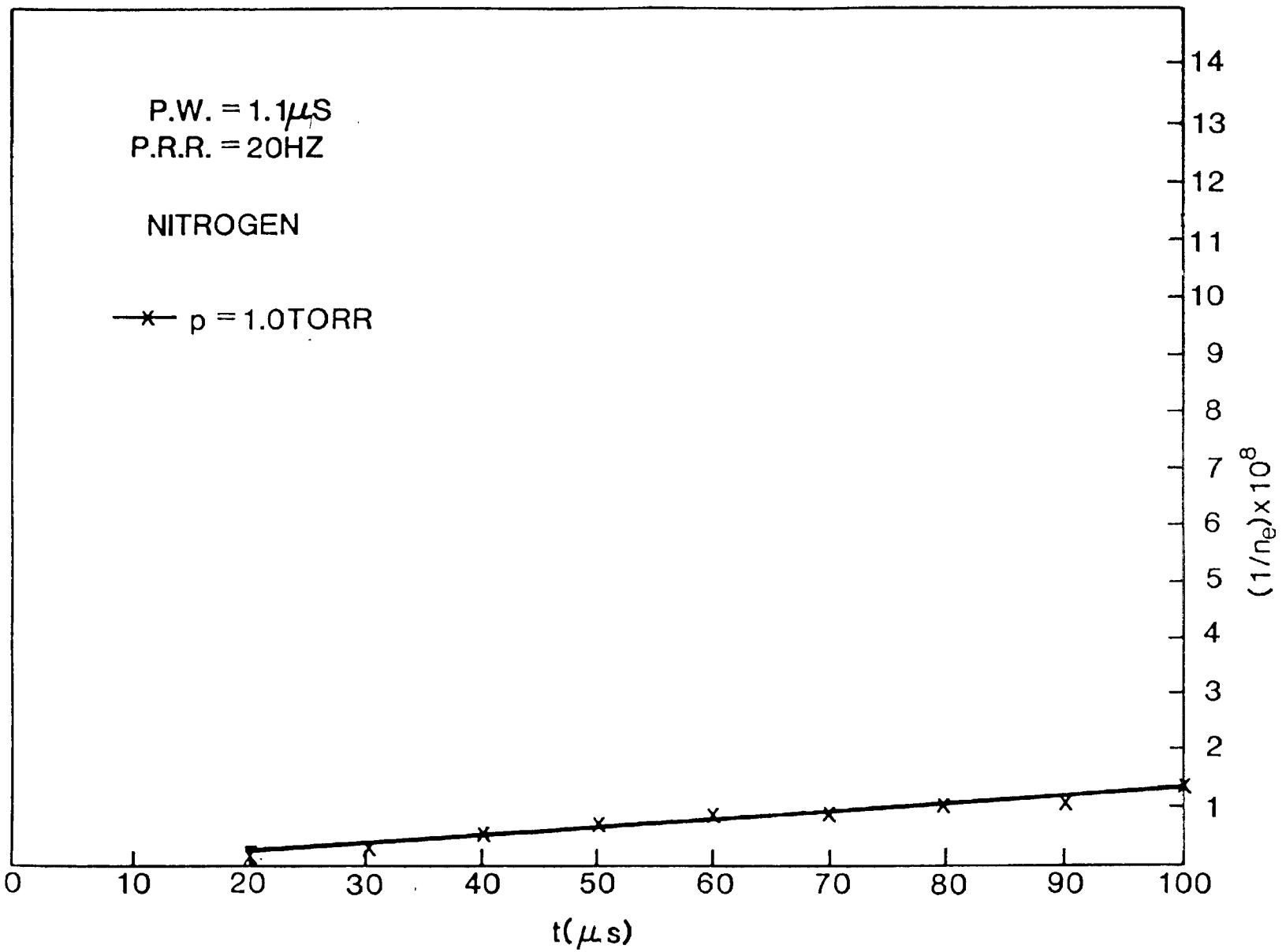

Figure 21(b). Plasma decay between 20 and 100μsec after the microwave pulse